




Atmospheric Flow at Alcantara Launch Center

Karine Klippel^{1,*} , Elisa Valentim Goulart¹ , Gilberto Fisch² , Bruno Furieri¹ , Cayo Prado Fernandes Francisco³ , Neyval Costa Reis Junior¹ 

1. Universidade Federal do Espírito Santo  – Centro Tecnológico – Programa de Pós-Graduação em Engenharia Ambiental – Vitória/ES – Brazil. **2.** Universidade de Taubaté  – Departamento de Ciências Agrárias – Taubaté/SP – Brazil. **3.** Departamento de Ciência e Tecnologia Aeroespacial  – Instituto de Aeronáutica e Espaço – São José dos Campos/SP - Brazil

*Correspondence author: karineklippel@gmail.com

ABSTRACT

The Alcantara Launch Center (ALC) is the main Brazilian access to space. It is positioned over a complex terrain, and it has some important buildings for assembling, integration and launching activities, such as the Mobile Integration Tower. Being in a region of prevalent trade winds, the flow interaction between the complex terrain and the buildings can affect the safety of operations on the platform, and the dispersion of toxic gases emitted during the launching. The main objective of this work was to study the influence of topography and buildings on the atmospheric flow of ALC using computational fluid dynamics (CFD) techniques. Three geometries were considered: simplified terrain (case 1), smooth complex terrain (case 2), and roughness complex terrain (case 3). The flow conditions over ALC were simulated using the ANSYS Fluent 19.0 CFD commercial code. The numerical simulations used a realizable κ - ϵ to model turbulence effects and the results presented a good agreement with the in-situ field measurements for the most complex geometry (case 3). The topography clearly influences the flow pattern at ALC, with the cliff influence over the wind being the major cause for establishing the flow patterns.

Keywords: Atmospheric flow; Complex terrain; Coastal cliff; Computational fluid dynamics (CFD); Atmospheric turbulence; Rocket launching.

INTRODUCTION

The Alcantara Launch Center (ALC), located in the northeastern Brazil, is the leading country gateway to space (Fig. 1). The launch pad area (called SPL) is positioned 150 m from the coastline, on a jagged cliff, with approximately 40 m height. Therefore, the change in roughness (smooth surface at the ocean to the rough surface at the continent) and the abrupt topography variation caused by the cliff can affect the atmospheric flow in the region and modify the flow properties of the planetary boundary layer. As a result, the flow from the ocean to the continent is disturbed and the flow properties of the planetary boundary layer are modified. Uchida and Ohya (2003) observed that local accelerations of the wind and separation regions of the boundary layer can be formed in flows over complex topographies, which affects the safety of operations on the platform as, for example, the dispersion of toxic gases emitted during launching.

Received: Mar. 27, 2021 | Accepted: Nov. 3, 2021

Peer Review History: Single-Blind Peer Review

Section editor: Juan Pablo Salazar



This is an open access article distributed under the terms of the Creative Commons license.



Figure 1. Aerial photography of the Brazilian rocket launch site. The Mobile Integration Tower (identified as TMI) location is indicated. Source: Retrieved from AEB (2019).

The launching platform has some buildings nearby necessary for assembly, integration, and launching activities— the Mobile Integration Tower, also known as TMI from its Portuguese name, the exit safety tower, and the control room (bunker), with the TMI and the exit tower being the tallest ones, with 33 and 25 m height, respectively. The flow around bluff obstacles is dominated by shear-generated mechanical turbulence. Therefore, the presence of buildings modifies the flow pattern causing the formation of characteristic flow features as separation and recirculation zones and turbulent wakes behind the obstacles (Arya 2001).

One of the major impacts related to the launch of rockets is the high rate of pollutant release almost instantaneously that can cause risks to human health (National Research Council 1998). The rocket engines launched at the ALC, including the satellite launch vehicle, work by burning solid propellant based on aluminized ammonium perchlorate. The combustion products are composed of toxic gases such as carbon monoxide (27.6%) and hydrogen chloride (21.6%). Schuch and Fisch (2017) did an analysis of the influence of this emission at ALC for a long-range dispersion forecast (higher than 5 km) while Klippel (2020) did for short range forecast (lower than 1 km). Furthermore, such analyses are of great importance in the cases of launching accidents that would result in larger amounts of pollutant gases.

Iriart and Fisch (2016) and Schuch and Fisch (2017) observed that the wind advection is a major meteorological factor that influences the pollutants dispersion at the ALC. Therefore, the knowledge of the flow pattern is essential to establish the atmospheric dispersion conditions to which the ALC is exposed and provide the necessary basis for studies of the dispersion of pollutants emitted during rocket launches.

In this context, the atmospheric flow at the ALC was studied using different approaches since the beginning of its activities. Field measurements provided the basis for understanding the flow patterns in the region, and wind tunnel experiments and numerical simulations provided more details about the flow characteristics in the region (Couto and Fisch 2018; Marciotto *et al.* 2012; Medeiros *et al.* 2013; Ramos *et al.* 2018).

Wind tunnel tests were also developed using simplifications of the local geometry like flat and smooth terrain (Faria *et al.* 2019; Pires *et al.* 2010; 2009). In these experiments, the abrupt change of topography was considered representing the cliff as a step with different inclinations. However, this is a rough representation of the local topography, as the cliff is very irregular and heterogeneous, a characteristic geographic feature in the ALC region. Several authors have studied atmospheric flow over complex terrains to understand the effects of topography on wind velocity and to predict, for example, the dispersion of pollutants in these regions (Balogh *et al.* 2012; Blocken *et al.* 2015; Hanjalić and Kenjereš 2005; Liu *et al.* 2016; Sharma *et al.* 2020; Tang *et al.* 2019; Yan *et al.* 2016; Yang *et al.* 2018; Yim *et al.* 2014).

Several of these studies have used computational fluid dynamics (CFD) techniques, based on two different approaches to turbulence modelling, Reynolds-average Navier–Stokes (RANS) and the more computationally demanding large eddy simulations (LES).

In the case of RANS simulations distinct closure models were adopted by different authors (Balogh *et al.* 2012; Sharma *et al.* 2020; Tang *et al.* 2019; Yim *et al.* 2014; Yan *et al.* 2016). In particular, the RANS κ - ϵ turbulence models showed good results when compared to field measurements (Balogh *et al.* 2012; Blocken *et al.* 2015; Gant and Tucker 2018; Tang *et al.* 2019; Yan *et al.* 2016) due to their inherently ability to deal with separated flows. Few studies have been conducted using numerical simulations

considering the ALC (Pires *et al.* 2011; Souza *et al.* 2015). Thus, new studies using computational simulations are important as they allow the detailed investigation of flow properties, sometimes not available from field or experimental measurements, besides the spatial description of the velocity and turbulence fields that define the atmospheric flow.

In this context, the main objective of this study was to simulate the atmospheric flow over the complex terrain of the ALC on scales not achievable by atmospheric models, using CFD techniques and inserting elements that represent the structure and the topography of the site under the influence of atmospheric turbulence. It is the first paper of a more comprehensive analysis of the short range (lower than 1 km) dispersion of HCl at ALC. The long-range dispersion (greater than 5 km) has been studied by Schuch and Fisch (2017) using a different type of model (in this case was an atmospheric mesoscale WRF model).

COMPUTATIONAL DOMAIN

Numerical simulations were conducted for three different representations of the ALC topography, namely, cases 1, 2 and 3. In the first geometry (case 1, Fig. 2a) a flat and smooth terrain is assumed, with the 40-m height coastal cliff represented by 90° steps. This simplified representation was considered, essentially, to evaluate the evolution of the refinement of geometry and its influence on atmospheric flow compared with field measurements.

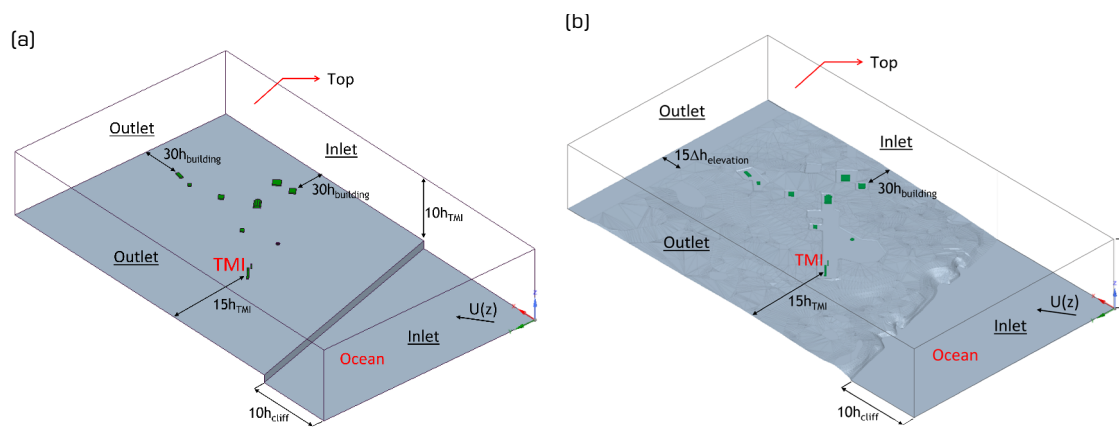


Figure 2. Computational domain. (a) Case 1; (b) Case 3. The TMI location is indicated. Domain boundaries were defined by the distance from the highest obstacle at each boundary ($h_{TMI} = 33$ m, $h_{cliff} = 40$ m, $h_{building} = 6$ m and $\Delta h_{elevation} = 6$ m). $U(z)$ arrow indicates the wind flow direction (70°, NNE). Source: Elaborated by the authors.

The geometry for cases 2 and 3 was more refined and considered the natural geographic complexity of the terrain, including the irregular and heterogeneous cliff on the ocean-continent interface. The topographic model was built based on the global digital topography model provided by the Japan Aerospace Exploration Agency, which has a 30-m spatial resolution (JAXA 2019). Despite the low resolution of the data, the data closely represents the ALC region when compared to the photographic pictures of the site (Fig. 1). The computational domain for cases 2 and 3 is presented in Fig. 2b. Domain boundaries were defined by the distance from the highest obstacle at each boundary. The total height of the domain is $10 h_{TMI}$ ($h_{TMI} = 33$ m).

The difference between cases 2 and 3 is that the influence of the presence of the local vegetation is considered only at case 3. According to IBGE (2019), the ALC is covered by a *restinga* ecosystem (coastal vegetation), with Fisch (1999) and Medeiros *et al.* (2013) referring to dense vegetation about 3 m height in the region. Then, the vegetation was represented as an elevation of 3 m from the surface, where it is present. This approach was adopted because the vegetation in the ALC region is very dense and acts as a solid barrier. Moreover, due to wall treatment implemented in the numerical simulations, representing the vegetation only as a surface roughness would require the use of very small control volumes, which would make it impossible to use a higher resolution mesh with the computational resources available for this study.

Figure 3 presents the altitude variation along the developed topographic model for case 3. It may be seen that all over the cliff extension, the altitudes vary between 12 and 26 m relative to the sea level. At the left and right sides, the topography is very irregular with the presence of small hills, mainly along the right side, with elevation varying from 12 to 41 m.

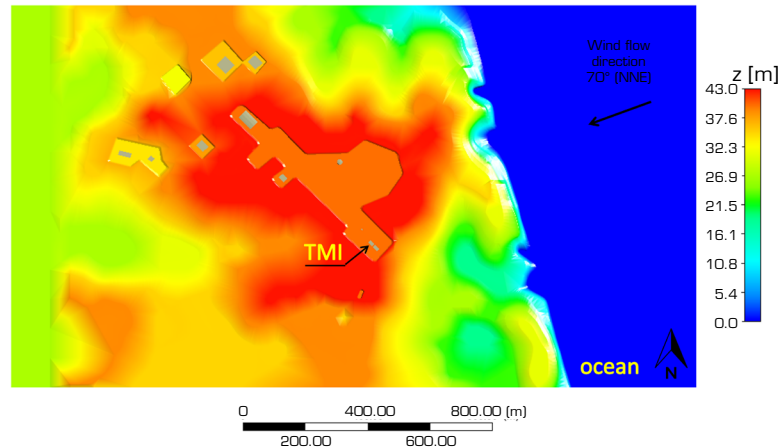


Figure 3. Plan view of altitude variation along the domain for case 3. The location of buildings is shown in grey. The TMI is indicated. The origin of the rectangular coordinate system was set at the top right. The wind flow direction (70° , NNE) is indicated by the arrow. Source: Elaborated by the authors.

The highest region in the domain is around the launch pad area (SPL), with about 43 m height. However, the SPL, where the TMI is located and from where the launching activities take place, has 40 m of elevation in relation to the sea level. Since the SPL presents a smaller elevation, its surroundings may influence the atmospheric flow at the site.

The main buildings which were identified in the study domain were considered in the three cases (Fig. 4).

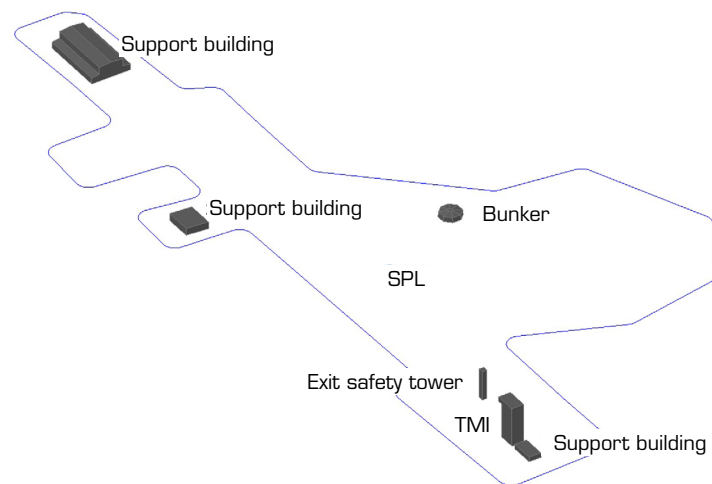


Figure 4. Main buildings of the launch pad area (SPL) considered in the domain. Source: Elaborated by the authors.

MATHEMATICAL MODELING

The simulations were conducted using RANS equations for incompressible and steady flow (Eqs. 1 and 2):

$$\frac{\partial \bar{u}_i}{\partial x_j} = 0 \quad (1)$$

$$\frac{\partial (\bar{u}_i \bar{u}_j)}{\partial x_j} = -\frac{1}{\rho} \frac{\partial \bar{p}}{\partial x_i} + \nu \frac{\partial^2 \bar{u}_i}{\partial x_j^2} - \frac{\partial (\overline{u'_i u'_j})}{\partial x_j} \quad (2)$$

where ρ is the density of fluid ($\text{kg}\cdot\text{m}^{-3}$), \bar{u}_i is the average i -th velocity in ($\text{m}\cdot\text{s}^{-1}$), u'_i is the i -th velocity fluctuation in ($\text{m}\cdot\text{s}^{-1}$), \bar{P} is the mean mechanical pressure ($\text{N}\cdot\text{m}^{-2}$) and ν is the kinematic viscosity ($\text{m}^2\cdot\text{s}^{-1}$). The nonlinear terms ($\overline{u'_i u'_j}$) were solved using the κ - ε realizable turbulence model.

Turbulence modeling

The RANS κ - ε realizable closure model of Shih *et al.* (1995) used in this study is a turbulent viscosity model based on the Boussinesq analogy, where the Reynolds stresses are modeled as a turbulent viscosity related to the mean velocity gradients. The κ - ε realizable model was chosen because its ability to deal with shear layers and recirculating flows, being one of the most widely used and validated turbulence models with a variety of applications including environmental flows. Also, the realizable version of the model is known for its improved computational performance, while generally providing better predictions for flows involving boundary layers under strong adverse pressure gradients, zones of separation and recirculation, features that commonly occurs in the flow over bluff bodies, as is the case for the flow over the ALC buildings. The transport equations modeled for the turbulent kinetic energy (TKE) κ and dissipation ε are presented in Eqs. 3 and 4.

$$\frac{\partial \kappa \bar{u}_j}{\partial x_j} = \frac{\partial}{\partial x_j} \left[(\nu_t) \frac{\partial \kappa}{\partial x_j} \right] + P_\kappa - \varepsilon \quad (3)$$

$$\frac{\partial \varepsilon \bar{u}_j}{\partial x_j} = \frac{\partial}{\partial x_j} \left[\left(\frac{\nu_t}{\sigma_\varepsilon} \right) \frac{\partial \varepsilon}{\partial x_j} \right] + C_1 S \varepsilon - C_2 \frac{\varepsilon^2}{\kappa + \sqrt{\nu \varepsilon}} \quad (4)$$

where $C_1 = \max[0, 4.3, \eta/(\eta + 5)]$, $\eta = S\kappa/\varepsilon$, $S = \sqrt{2S_{ij}S_{ij}}$, P_κ is the TKE production term ($P_\kappa = \nu_t S^2$, $\text{N}\cdot\text{m}^{-2}\cdot\text{s}^{-1}$), S_{ij} is the strain rate tensor (s^{-1}), σ_κ and σ_ε are the turbulent Prandtl numbers and C_2 is an empirical constant of the model. The adopted constants were: $\sigma_\kappa = 1.0$, $\sigma_\varepsilon = 1.2$ and $C_2 = 1.0$ (ANSYS 2018).

In this study, the scalable wall function modified by the roughness (Launder and Spalding 1983) was used to ensure numerical accuracy of the results. The wall functions bridge the inner region between the wall and the fully developed region, eliminating the necessity to resolve the boundary layer and greatly reducing the mesh size. According to ANSYS (2018), the implemented scalable wall functions produce consistent results for meshes of arbitrary refinement. The nondimensional parameters necessary to calculate the first grid cell are (Eqs. 5 and 6):

$$y^+ = \frac{\rho u^* y_p}{\mu} \quad (5)$$

$$K_S^+ = \frac{\rho K_S u^*}{\mu} \quad (6)$$

where y^+ is the dimensionless distance from the wall, y_p is the distance from the center point P of wall-adjacent cell (m), u^* is the friction velocity ($\text{m}\cdot\text{s}^{-1}$), K_S^+ and K_S are the dimensionless and physical roughness height (m), respectively, and it must be emphasized that K_S is not equivalent to the z_0 aerodynamics roughness coefficient (Yan *et al.* 2016). For a fully turbulent flow, K_S is much larger than the corresponding z_0 and can be approximated to $30z_0$. The distance from the center point P of the wall-adjacent cell to the wall must be at least twice the physical height of roughness ($y_p > K_S$) (ANSYS 2018; Antonini *et al.* 2019; Blocken *et al.* 2007).

In order to not compromise the fine grid resolution, in case 3, vegetation was represented as an elevation of 3 m and was considered as a small aerodynamic roughness coefficient ($z_0 = 0.02$ m corresponding to $K_S = 0.6$ m). In the cliff, built areas and

the ocean K_s was equal to 0.6, 0.03 and 3×10^{-4} m, respectively. The walls of the buildings were considered to be smooth surfaces, where the no-slip condition was applied.

While this work uses the κ - ϵ turbulence model for atmospheric simulations, another parallel work has been conducted using the LES model technique (Couto 2020).

Boundary conditions

The boundary conditions adopted for the simulations were: (i) inlet, in situ data-based velocity profile and constant turbulent intensity; (ii) outlet, zero static gauge pressure; (iii) top, free slip condition (zero shear stress); (iv) floor and building walls, no-slip condition ($u_i = 0$).

The inlet velocity profile was defined based on the final analysis data of the National Centers for Environmental Prediction. The data were obtained for September 20, 2008 (representing the dry period), at 00:00 h (UCT). Usually, the Brazilian rockets are launched during the dry period in order to avoid problems with rainfall. Also, this period was chosen to compare the final analysis data set with radiosondes observations made at the ALC. The velocity profile was interpolated by a logarithmic law based on the similarity theory for neutral surface layer (Eq. 7). The logarithmic profile coefficients were $u^* = 0.4 \text{ m}\cdot\text{s}^{-1}$ and $z_0 = 3.0 \times 10^{-4} \text{ m}$.

$$u(z) = \left(\frac{u^*}{\kappa_*}\right) \ln\left(\frac{z}{z_0}\right) \quad (7)$$

The mean inlet velocity was $11.5 \text{ m}\cdot\text{s}^{-1}$. The reference Reynolds number (Re) was 2.5×10^7 , with a characteristic length corresponding to the TMI height (33 m). The incident velocity direction was 70° (North-Northeast, NNE, mean wind direction obtained by reanalyzed data), which agrees with the prevailing winds of the ALC: northeast and east winds (Fisch 2010; Medeiros *et al.* 2013).

Some tests were carried out and the inlet turbulence intensity obtained for the convergence and validation of the simulation was determined by 5% (κ and ϵ were $0.17 \text{ m}^2\cdot\text{s}^{-2}$ and $2.80 \cdot 10^{-4} \text{ m}^2\cdot\text{s}^{-2}$, respectively), the same value obtained for the wind tunnel measurements (Faria *et al.* 2019) and close to observational values obtained by Fisch (1999).

NUMERICAL METHODS

The present study was developed using the finite volume based on CFD commercial software ANSYS Fluent 19.0. The computational mesh representing the simulation domain was composed predominantly by hexahedral elements. The elements adjacent to the ground (ocean, cliff and continent) were 1.2 m, with a growth rate of 1.2.

Close to the walls of the main buildings the elements size was 0.6 m, with a growth rate of 1.2. In these regions, a layer of prismatic elements was inserted to better resolve the near wall flow. The first prismatic layer had 0.01 m, resulting in y^+ less than 200, appropriate for the use of turbulence wall functions, with growth rate of 1.5 for a total of six layers. Grid sensitivity tests were performed and acceptable results for the chosen mesh and methods were found. The total number of nodes (elements) of the computational meshes were 14,281,481 (12,424,099), 15,311,238 (13,520,297) and 15,449,500 (13,663,248) for cases 1 to 3, respectively. Figure 5 shows the computational mesh for case 3, highlighting the TMI and coastal cliff details.

The first order upwind scheme was used for the discretization of the momentum, κ and ϵ equations and, although being known for its propensity to numerical diffusion, it was necessary for stability. To solve the Navier–Stokes equations the iterative Semi-Implicit Method for Pressure Linked Equations (SIMPLE) algorithm, described by Patankar (1980), was employed for the pressure-velocity coupling solution. The iterative convergence criteria used was that the solution was well converged when the root mean square residuals reached the limit of five decimal digits.

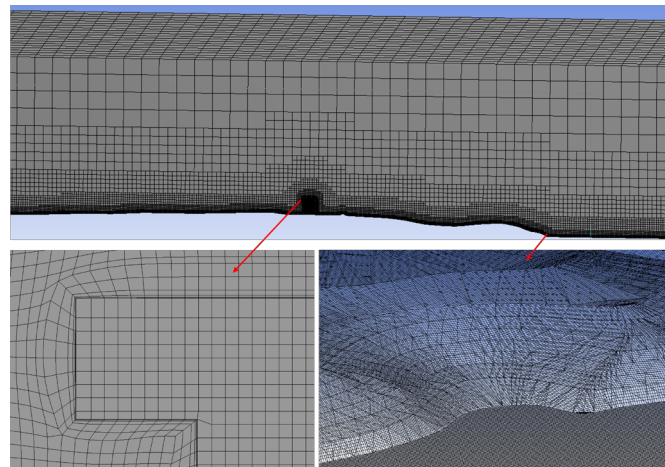


Figure 5. Mesh for case 3, presenting some details of the TMI and the coastal cliff. Source: Elaborated by the authors.

RESULTS AND DISCUSSION

In a neutral atmosphere, the flow is modified mainly due to the shear stresses generated due to its interaction with the walls of the domain (surface and faces of the buildings). Figure 6 shows the mean longitudinal velocity and streamlines over the cliff for the three cases analyzed, considering the direction of the prevailing mean flow. For case 1 (Fig. 6a) the flow reaching the step (cliff) causes a separation zone. The velocities in $0.3 h_{TMI}$ and $0.6 h_{TMI}$ above the cliff were 9.4 and $10.6 \text{ m}\cdot\text{s}^{-1}$, respectively. A reverse flow region is formed upstream the obstacle with velocities below $2.5 \text{ m}\cdot\text{s}^{-1}$ and negative velocities close to $-1.0 \text{ m}\cdot\text{s}^{-1}$.

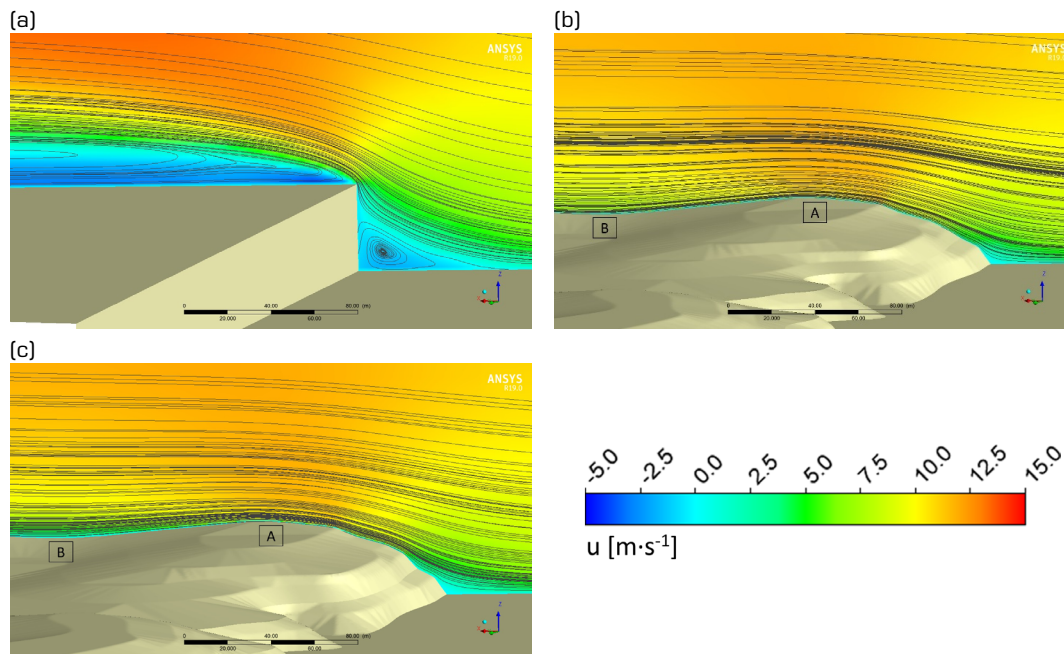


Figure 6. Streamlines on the cliff. (a) Case 1; (b) Case 2; (c) Case 3; A indicates the highest point on the cliff and B indicates the lowest point just after the cliff. Source: Elaborated by the authors.

As obtained by Faria *et al.* (2019), downstream the cliff is a recirculation zone that extends up to the TMI. This behavior of the flow crossing a step were also observed in Essel and Tachie (2017) and in Wu and Ren (2013). As in the present study, these studies showed that two recirculation zones are formed, upstream and downstream to the step. It has also been observed that its intensity and extension depend on some conditions such as the flow Re, the surface roughness before and after the step and its height. In Essel and Tachie (2017), considering smooth surfaces, it has been found that the increase in the Re induce an intensification of the recirculation zone downstream the step. In the present work, the Re is higher (107), which may have favored the intensity of the recirculation downstream the step.

In Wu and Ren (2013) it has been observed that on rough and irregular surfaces, the recirculation zone downstream the step tends to be attenuated. In cases 2 and 3 (Fig. 6b and c), adding the real topography, the flow followed the cliff geometry smoothly, and the separation and recirculation zones downstream the cliff were smaller when compared to case 1.

For cases 2 and 3, although near the surface the velocity is zero due to the boundary condition (no-slip), the flow is accelerated on the cliff and the maximum velocities was 11.3 and 11.7 $\text{m}\cdot\text{s}^{-1}$ for case 2 and 11.8 and 12.4 $\text{m}\cdot\text{s}^{-1}$ for case 3 at $0.3 h_{\text{TMI}}$ and $0.6 h_{\text{TMI}}$ above the cliff (at the highest altitude of the cliff identified by the letter A in Fig. 6b and 6c). In both cases, punctual locations of flow acceleration and deceleration were observed along the topography. Right after the cliff (identified by the letter B in the figures), there is a small drop in the terrain where the flow has lower velocities. In the first 5 m height from ground level, the velocities varied between 0.0 and 5.7 $\text{m}\cdot\text{s}^{-1}$ in case 2, and between 0.0 and 4.1 $\text{m}\cdot\text{s}^{-1}$ in case 3. The velocities close to the ground were lower for case 3, which is justified by the presence of surface roughness, which causes the displacement of the velocity profile and decelerate the flow close to the surface.

Figure 7 shows the TKE contours over the cliff for cases 1 to 3. The TKE fields follow the same patterns as the velocity fields for case 1 (Fig. 7a). The highest values of TKE are observed in the separation of the boundary layer with maximum value of $7.3 \text{ m}^2\cdot\text{s}^{-2}$. This is due to the high average velocity gradients formed in this region, which cause the flow instability and the separation of the shear layer (Saeedi *et al.* 2014). In case 3a (Fig. 7b), TKE is higher in the highest altitude of the cliff, where there is an acceleration of the flow, reaching $3.3 \text{ m}^2\cdot\text{s}^{-2}$, which is lower than the values of case 1. TKE values for case 2 were below $0.5 \text{ m}^2\cdot\text{s}^{-2}$ and their images were not presented.

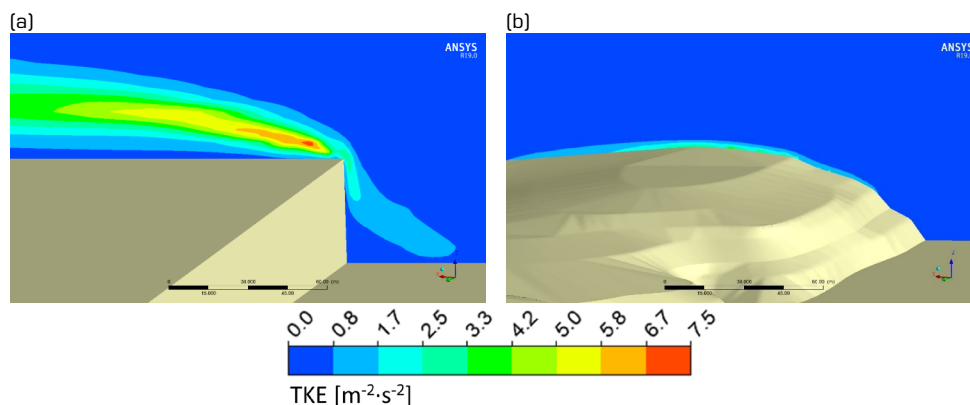


Figure 7. Turbulent kinetic energy around the cliff: (a) case 1 and (b) case 3. Source: Elaborated by the authors.

Figure 8a, c and e shows the average velocity vectors around the TMI for the three cases, considering a longitudinal plane in the flow direction. For case 1 (Fig. 8a), the separate flow on the cliff did not reach the reattachment point when it arrived at the building. Then, the obstacle interacts with a fully turbulent separated flow with high turbulence intensity. Two recirculation zones with low velocities are observed: upstream and downstream the TMI. At $0.5 h_{\text{TMI}}$ upstream, the velocities varied between -1.1 and $4.2 \text{ m}\cdot\text{s}^{-1}$. At $0.5 h_{\text{TMI}}$ downstream, the velocities ranged between 0.0 and $2.3 \text{ m}\cdot\text{s}^{-1}$. The velocities around the building are lower in this situation when compared to the other cases.

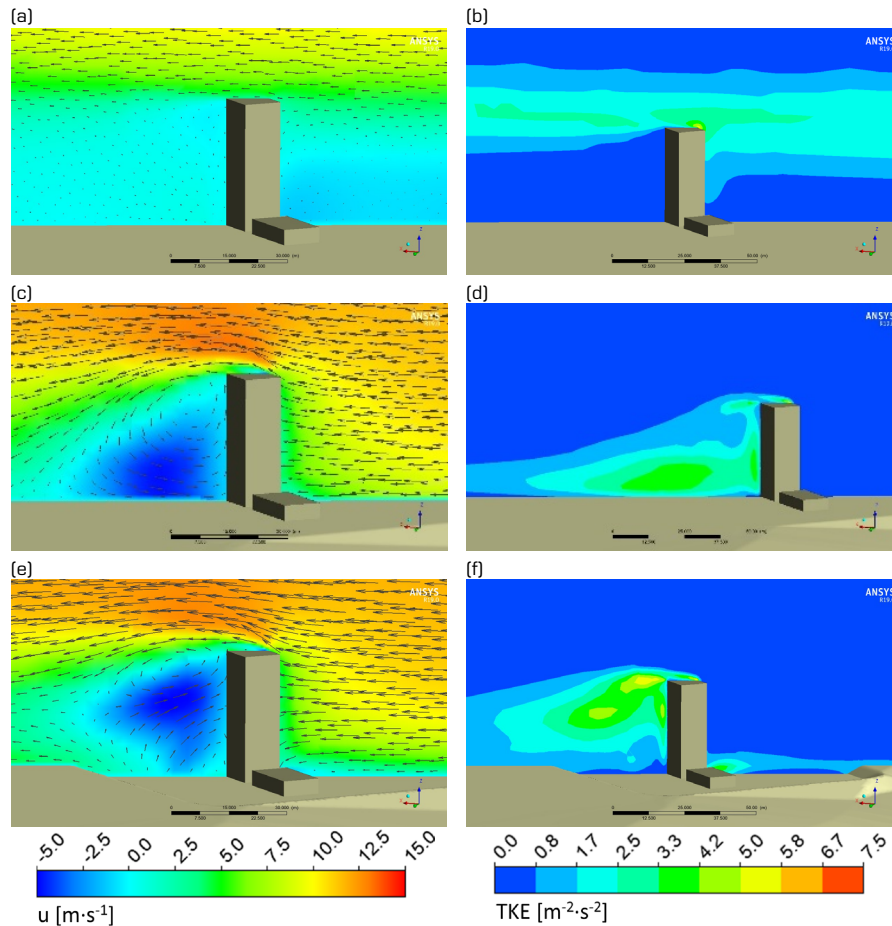


Figure 8. Velocity vectors and TKE contours around the TMI: (a, b) case 1, (c, d) case 2 and (e, f) case 3. Source: Elaborated by the authors.

For cases 2 and 3 (Fig. 8c and e) some typical characteristics of the flow around a square cylinder obstacle are observed. The incident flow on the TMI is separated causing a stagnation zone. At the upper edge it is accelerated and detached from the building, where a reverse flow is formed on the top. Behind the building, it is possible to observe the tendency of the flow to reattach. A recirculation zone is formed behind the obstacle, characterized by negative velocity values. This flow pattern was also observed in flow studies around tall buildings (Joubert *et al.* 2015; Saeedi *et al.* 2014). For case 2, at $0.5 h_{TMI}$ upstream, the TMI the velocities varied between 0.0 and $9.5 \text{ m}\cdot\text{s}^{-1}$; for case 3, between 0.0 and $11.2 \text{ m}\cdot\text{s}^{-1}$ (in $0.5 h_{TMI}$). The velocities close to the ground upstream the building was lower for case 3, which is justified by the presence of the surface roughness. The roughness causes the displacement of the velocity profile and decelerates the flow close to the surface. The pattern of the recirculation zone behind the TMI showed differences for cases 2 and 3. For case 2 there was a single reverse flow zone, centered at the upper region of the building; whereas for case 3 two reverse flow zones were observed, one centered at the upper part of the obstacle and another in the lower part. At $0.5 h_{TMI}$ upstream, the velocities varied between -4.2 and $7.3 \text{ m}\cdot\text{s}^{-1}$ for case 2 and between -3.5 and $7.3 \text{ m}\cdot\text{s}^{-1}$ for case 3.

Figure 9 shows the xy (horizontal) plane at $z = 0.5 h_{TMI}$. For all cases, it can be observed the formation of low-velocity recirculation zones behind the TMI and the exit safety tower, with two asymmetric vortices and different characteristics. For case 1 (Fig. 9a) the velocities are lower when compared to the other cases, while the representation of the cliff by a step changes the predominant wind direction (70° inlet) near the TMI. For cases 2 and 3 (Fig. 9b and c) the wake is more widely spread behind the TMI and exhibits complex vortex motions. For case 2 the highest velocities in the horizontal plane are observed.

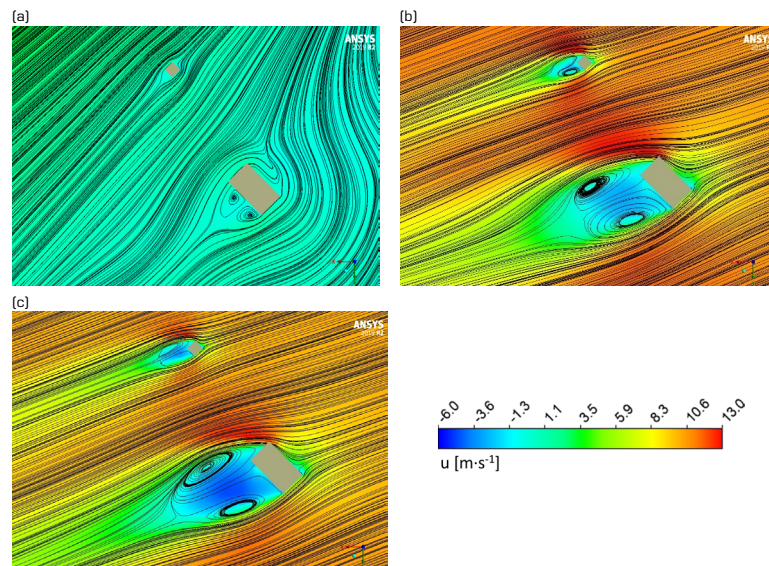


Figure 9. Streamlines around the TMI: a) case 1, b) case 2 and c) case 3. Source: Elaborated by the authors.

Figure 8b, d and f shows the contours of TKE around the TMI in the flow direction. Comparing Fig. 8a and b, it is observed that for case 1 the highest TKE values are in the flow separation zone on the cliff. Around the building (Fig. 8b), the highest values were observed at the upper edge of the front face, where there is a small separation of the boundary layer. In this region the maximum TKE is around $5.0 \text{ m}^2\cdot\text{s}^{-2}$.

Differently from case 1, for cases 2 and 3 (Fig. 8d and f) the highest TKE values occurred in the separation and recirculation zones of the flow around the TMI. For case 2 (Fig. 8d), the maximum TKE values were $6.0 \text{ m}^2\cdot\text{s}^{-2}$ in the separation zone and $4.1 \text{ m}^2\cdot\text{s}^{-2}$ in the recirculation zone. For case 3 (Fig. 8f), the maximums in those same regions were 4.4 and $5.7 \text{ m}^2\cdot\text{s}^{-2}$ in the separation and recirculation zones, respectively. Behind the building, TKE was higher in the lower region, closer to the ground, for case 2 and in the upper region, closer to the top of the building, for case 3.

Some velocity profiles (identified by T1 to T6) were obtained along the longitudinal xz plane for cases 1 to 3 (Fig. 10). Figure 11a shows that the flow is disturbed by the presence of the cliff. For case 1, below $0.8 z\cdot\text{h}^{-1}_{\text{TMI}}$ the velocities varied between -0.1 and $0.8 u/\bar{U}$ and were smaller compared to the inlet profile, which for the same height has velocities from 0.7 and $0.9 u/\bar{U}$. Above $0.8 z\cdot\text{h}^{-1}_{\text{TMI}}$ the flow is accelerated and the velocities are higher compared to the inlet profile.

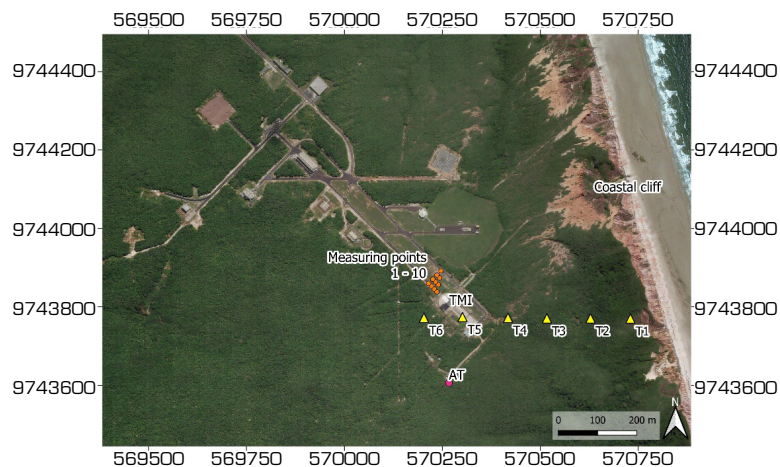


Figure 10. Location of the T1–T6 points (yellow triangles), the measuring points 1 to 10 by Marciotto *et al.* (2012) (orange circles) and the anemometric tower (AT, pink circle). The TMI is indicated on the map. Source: Elaborated by the authors.

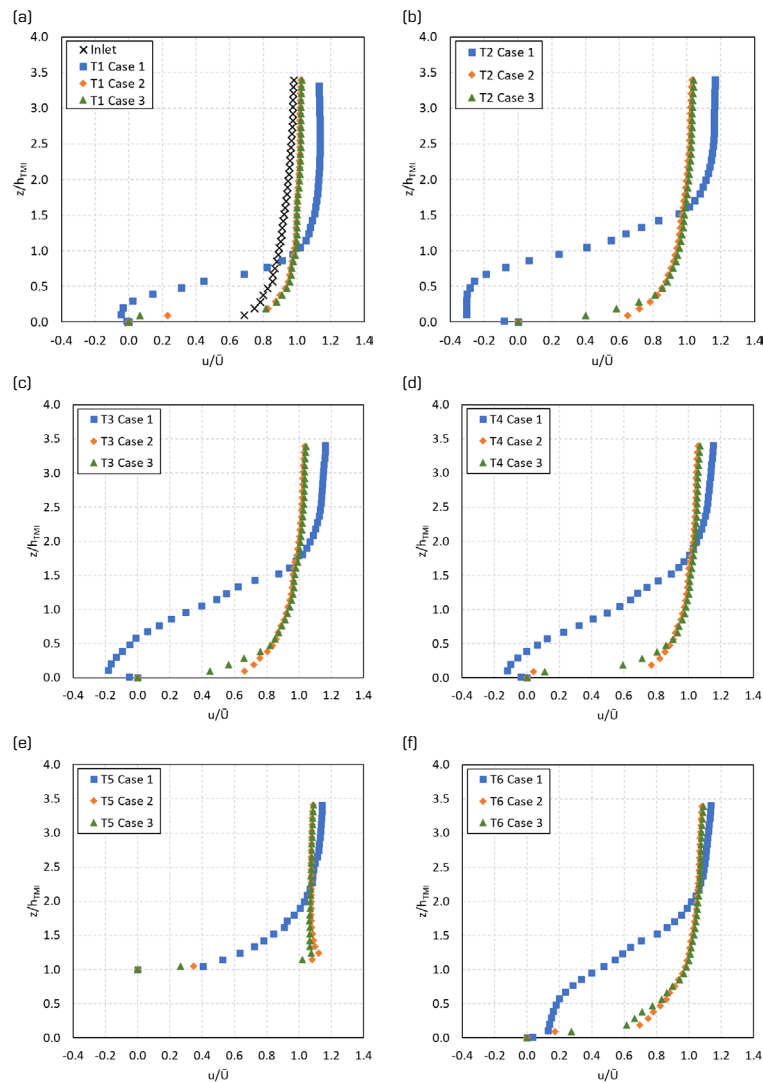


Figure 11. Mean velocity profiles in xz plane. (a) Position T1; (b) Position T2; (c) Position T3; (d) Position T4; (e) Position T5; (f) Position T6. h_{TMI} is the height of the TMI (33 m) and \bar{u} is the average inlet velocity ($11.5 \text{ m}\cdot\text{s}^{-1}$). Source: Elaborated by the authors.

In cases 2 and 3, the profiles are modified when passing through the cliff, but less accentuated when compared to case 1. In both cases, the same behavior of the inlet profile is observed; however, with higher velocities above $0.2 z\cdot h^{-1}_{TMI}$. When passing through the cliff, the flow is accelerated and reaches velocities of $0.9 u/\bar{u}$ for both cases at $0.5 z\cdot h^{-1}_{TMI}$.

Upstream the cliff, the velocity at $0.5 z\cdot h^{-1}_{TMI}$ is $0.8 u/\bar{u}$. That is, an increase of over $0.1 u/\bar{u}$. In general, the same pattern was observed in Pires *et al.* (2010). The authors observed that on the cliff, the mean flow is disturbed and accelerated.

The topography along the domain also causes changes in the profiles, mainly close to the ground. However, in the three cases the presence of the cliff was the major cause for changing of the atmospheric flow at the ALC.

All profiles in Fig. 11 presented very similar results for cases 2 and 3, especially above $0.5 z\cdot h^{-1}_{TMI}$. Below $0.5 z\cdot h^{-1}_{TMI}$, which is closer to the ground, the velocities for case 3 are lower than for case 2. The surface roughness causes a displacement of the profile and decelerate the velocities on the surface.

The velocities for case 1 are higher compared to cases 2 and 3 for upper heights. Throughout the domain, this difference decreases. In T6 profile (Fig. 11f), after the TMI, the velocities above $2.0 z \cdot h^{-1}_{TMI}$ for all cases are close to $1.0 u/\bar{U}$.

Considering the profile above the TMI (Fig. 11e), for case 1, the presence of the building did not cause significant changes in the velocity profile. For cases 2 and 3 the flow is accelerated by the presence of the obstacle. This acceleration is more accentuated in case 2, with velocities around $0.1 u/\bar{U}$ higher for this case.

A final analysis was made comparing the results of the numerical simulations with the field measurements of Marciotto *et al.* (2012) (Table 1). All points are located near the launch pad (Measuring points 1–10, orange circles, in Fig. 10). They were obtained from 10 anemometers installed on 10-m-high masts arranged in a triangular mesh with a spacing of 10 m. According to Table 1, the measured velocities are in general spatially homogeneous. The lower velocity was measured in point 1 ($7.5 \text{ m}\cdot\text{s}^{-1}$), while the larger velocity was measured in point 10 ($9.6 \text{ m}\cdot\text{s}^{-1}$). The difference between them is of $2.1 \text{ m}\cdot\text{s}^{-1}$. The velocities in the other points vary from 8.0 to $8.9 \text{ m}\cdot\text{s}^{-1}$.

Table 1. Comparison between the field observational data (U_{obs}) and the results from the numerical simulations (U_{sim}) for cases 1, 2 and 3 using the model κ - ϵ . Error is the relative error between the results, given in %.

Points	$U_{obs} \text{ (m}\cdot\text{s}^{-1}\text{)}$	$U_{sim} \text{ (m}\cdot\text{s}^{-1}\text{)}$			Error (%)		
		Case 1	Case 2	Case 3	Case 1	Case 2	Case 3
1	7.5	3.7	11.3	8.6	50.2	50.5	14.3
2	8.3	4.0	11.3	8.5	52.1	35.4	1.8
3	8.2	4.2	11.2	8.4	48.6	36.4	1.9
4	8.0	4.5	11.2	8.3	44.4	39.1	3.5
5	8.3	4.0	11.2	8.6	52.0	36.0	4.5
6	8.2	4.2	11.2	8.5	49.0	35.7	3.5
7	8.3	4.4	11.1	8.5	46.7	33.5	1.5
8	8.6	4.2	11.1	8.6	51.7	28.9	0.4
9	8.9	4.4	11.1	8.6	50.2	24.8	3.5
10	9.6	4.7	11.0	8.7	54.3	14.8	9.5
Ave	8.4	7.2	11.2	8.5	49.9	33.5	4.4
Min	7.5	3.7	11.0	8.3	44.4	14.8	0.4
Max	9.6	4.5	11.3	8.7	54.3	50.5	14.3

Source: Elaborated by the authors.

Spatial homogeneity has also been seen in the numerical simulations. The numerical results presented velocities varying from 3.7 to $4.7 \text{ m}\cdot\text{s}^{-1}$ for case 1, from 11.0 to $11.3 \text{ m}\cdot\text{s}^{-1}$ for case 2, and from 8.3 to $8.7 \text{ m}\cdot\text{s}^{-1}$ for case 3. The simulated velocities in case 1 were the most discrepant compared to the measured velocities, followed by case 2. The minimum relative errors for cases 1 (44.4%) and 2 (14.8%) were greater than the maximum relative error obtained for case 3 (14.3%). The maximum relative errors for the first cases exceeded 50.0%.

It was also possible to analyze the results of cases 1 to 3 in comparison with the measurements of the ALC anemometric tower, identified by AT in Fig. 10. Figure 12 shows that the velocity profile calculated for case 1 had a very divergent behavior in relation to the profile of the anemometric tower. The insertion of the real topography (cases 2 and 3) improved its performance, but the numerical simulations overestimate the velocities. Comparing cases 2 and 3, it is clear that vegetation provided a reduction between 2 and $3.5 \text{ m}\cdot\text{s}^{-1}$ in velocities close to the ground and, consequently, a better performance in relation to local measurements.

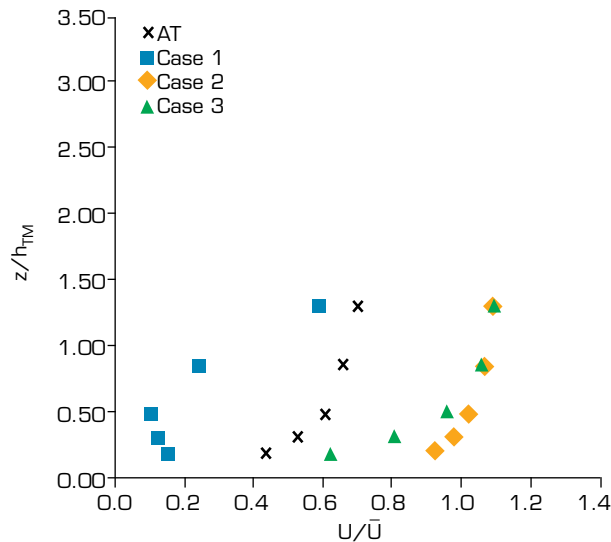


Figure 12. Comparison between the velocities measured by the anemometric tower of the ALC and the results from the numerical simulations for cases 1, 2 and 3. h_{TMI} is the height of the TMI (33 m) and \bar{U} is the average inlet velocity ($11.5 \text{ m}\cdot\text{s}^{-1}$). Source: Elaborated by the authors.

For case 3, on average, the simulated velocities are $0.3 u/\bar{U}$ greater than that obtained by the field measurements, what is equivalent to a mean overestimation of $3.6 \text{ m}\cdot\text{s}^{-1}$. The relative mean error between the measurements and the simulations is 50.2%. The smaller relative error (32.0%) has been obtained at the higher measurement point ($3.3 z\cdot h_{TMI}^{-1}$, equivalent to an elevation of 110 m), while the greater relative error (60.9%) was obtained at the elevation of 28 m ($0.8 z\cdot h_{TMI}^{-1}$).

In the light of the analyses that were carried out, it was possible to conclude that incorporating the elements that characterize the surface of the ALC (topography and vegetation) into the numerical simulations is crucial to identify the flow patterns in the region. Simplifications can result in significant changes in the velocity fields and in the TKE.

CONCLUSION

It was observed that the topographic variation influenced the atmospheric flow in an important site of the ALC, the launch pad area (SPL). In all cases 1, 2 and 3, the cliff was the major responsible for changing this flow, especially for case 1, where it has been represented by a step (90°). For case 1, the atmospheric flow is separated when passing through the cliff and it is accelerated at the continent-ocean interface. Two recirculation zones are formed: upstream and downstream of the cliff. However, this configuration is unrealistic as it imposes a much more severe geometrical constraint to the flow. The atmospheric flow in SPL shows intense recirculation and lower velocities when the real cliff topography is used (cases 2 and 3).

Considering the situation where the real terrain topography is used (cases 2 and 3), the change in topography was less abrupt and, therefore, the flow follows the geometry of the cliff in a smooth way. Because of surface roughness the velocities close to the surface were lower for case 3 with the velocity profile being displaced causing a deceleration adjacent to the ground. The flow over the complex terrain is accelerated in specific locations, mainly where more significant variations in topography were observed. The numerical results presented a good agreement with the in-situ flow field measurements for the most complex geometry (case 3). The maximum relative error between the numerical results and the observations measurements was 14.3%.

The flow pattern is also modified by the interaction with the buildings and obstacles at SPL. At the TMI and the exit tower areas, vertical and lateral separation zones are formed by the flow, as they act as aerodynamically bluff bodies. The turbulent

wake behind the buildings is responsible for local vorticity generation forming coherent flow structures that can extend for many meters behind these bodies.

Finally, this is an initial part of a study about the influence and interaction among topography, local surface roughness and buildings/obstacles at the atmospheric flow at Alcantara Space Center. Another study, in preparation, will address the toxic gases dispersion released by normal launchings.

AUTHORS' CONTRIBUTION

Conceptualization: Klippel K, Goulart EV, Fisch G and Reis NC; **Analysis:** Klippel K, Goulart EV, Fisch G and Francisco CPF; **Writing – Original Draft:** Klippel K, Goulart EV, Fisch G and Furieri B; **Writing – Review and Editing:** Klippel K, Goulart EV, Fisch G, Furieri B and Francisco CPF; **Funding Acquisition:** Fisch G; **Resources:** Goulart EV and Fisch G; **Supervision:** Goulart EV and Fisch G;

DATA AVAILABILITY STATEMENT

The data will be available upon request.

FUNDING

Conselho Nacional de Desenvolvimento Científico e Tecnológico

DOI: [<https://doi.org/10.13039/501100003593>]

Grants Nos. 403899/2016-8 and 133209/2018-0

ACKNOWLEDGEMENTS

Not applicable.

REFERENCES

[IBGE] Instituto Brasileiro de Geografia e Estatística (2019) Geociências Informações Ambientais. Vegetação. Estado do Maranhão. [accessed Aug 20 2019]. <https://www.ibge.gov.br/geociencias/informacoes-ambientais/vegetacao/22460-vegetacao-por-estado.html?=&t=acesso-ao-produto>

[JAXA] Japan Aerospace Exploration Agency (2019) ALOS World 3D - 30m. [accessed Aug 20 2019]. <https://portal.opentopography.org/raster?opentopoID=OTALOS.112016.4326.2>

AEB (2019) Agência Espacial Brasileira. <https://www.gov.br/aeb/pt-br>. Accessed Feb 25 2019.

ANSYS (2018) ANSYS Inc. ANSYS Fluent 19.0 Theory Guide.

Antonini EGA, Romero DA, Amon CH (2019) Improving CFD wind farm simulations incorporating wind direction uncertainty. *Renew Energ* 133:1011-1023. <https://doi.org/10.1016/j.renene.2018.10.084>

- Arya PS (2001) Introduction to micrometeorology. San Diego: Academic Press. Vol. 79.
- Balogh M, Parente A, Benocci C (2012) RANS simulation of ABL flow over complex terrains applying an Enhanced k- ϵ model and wall function formulation: Implementation and comparison for fluent and OpenFOAM. *J Wind Eng Ind Aerodyn* 104-106:360-368. <https://doi.org/10.1016/j.jweia.2012.02.023>
- Blocken B, Stathopoulos T, Carmeliet J (2007) CFD simulation of the atmospheric boundary layer: wall function problems. *Atmos Environ* 41(2):238-252. <https://doi.org/10.1016/j.atmosenv.2006.08.019>
- Blocken B, van der Hout A, Dekker J, Weiler O (2015) CFD simulation of wind flow over natural complex terrain: Case study with validation by field measurements for Ria de Ferrol, Galicia, Spain. *J Wind Eng Ind Aerodyn* 147:43-57. <https://doi.org/10.1016/j.jweia.2015.09.007>
- Couto VM (2020) Simulação do escoamento e da camada limite no centro de lançamento de Alcântara (MA) utilizando modelo de grandes turbilhões (Doctoral Dissertation). São José dos Campos: Instituto Nacional de Pesquisas Espaciais. In Portuguese.
- Couto VM, Fisch G (2018) Análise espacial dos ventos no Centro de Lançamento de Alcântara, Maranhão. *Ciênc Nat* 40(Spec No):57-62. <https://doi.org/10.5902/2179460X30648>
- Essel EE, Tachie MF (2017) Upstream roughness and Reynolds number effects on turbulent flow structure over forward facing step. *Int J Heat Fluid Flow* 66:226-242. <https://doi.org/10.1016/j.ijheatfluidflow.2015.11.004>
- Faria AF, Avelar AC, Fisch G (2019) Wind Tunnel Investigation of the Wind Patterns in the Launching Pad Area of the Brazilian Alcântara Launch Center. *J Aerosp Technol Manag* 11:e0719. <https://doi.org/10.5028/jatm.v11.996>
- Fisch G (1999) Características do perfil vertical do vento no Centro de Lançamento de Foguetes de Alcântara (CLA). *Rev Bras de Meteorol* 14(1):11-21.
- Fisch G (2010) Comparisons between aerovane and sonic anemometer wind measurements at Alcântara Launch Center. *J Aerosp Technol Manag* 2(1):105-110. <https://doi.org/10.5028/jatm.2010.0201105110>
- Gant SE, Tucker H (2018) Computational Fluid Dynamics (CFD) modelling of atmospheric dispersion for land-use planning around major hazards sites in Great Britain. *J Loss Prev Process Ind* 54:340-345. <https://doi.org/10.1016/j.jlp.2018.03.015>
- Hanjalić K, Kenjereš S (2005) Dynamic simulation of pollutant dispersion over complex urban terrains: A tool for sustainable development, control and management. *Energy* 30(8):1481-1497. <https://doi.org/10.1016/j.energy.2004.05.001>
- Iriart PG, Fisch G (2016) Uso do Modelo WRF-CHEM para a Simulação da Dispersão de Gases no Centro de Lançamento de Alcântara. *Rev Bras Meteorol* 31(4 Suppl 1):610-625. <https://doi.org/10.1590/0102-7786312314b20150105>
- Joubert E, Harms TM, Venter G (2015) Computational simulation of the turbulent flow around a surface mounted rectangular prism. *J Wind Eng Ind Aerodyn* 142:173-187. <https://doi.org/10.1016/j.jweia.2015.03.019>
- Klippel K (2020) Estudo do escoamento atmosférico em microescala no Centro de Lançamento de Alcântara por meio de simulações numéricas (Master's Thesis). Vitória: Universidade Federal do Espírito Santo. In Portuguese.
- Launder BE, Spalding DB (1983) The numerical computation of turbulent flows. In: Patankar SV, Pollard A, Singhal AK, Vanka SP, editors. *Numerical Prediction of Flow, Heat Transfer, Turbulence and Combustion: Selected Works of Professor D. Brian Spalding*. Oxford: Pergamon Press. p. 96-116. <https://doi.org/10.1016/B978-0-08-030937-8.50016-7>
- Liu Z, Ishihara T, He X, Niu H (2016) LES study on the turbulent flow fields over complex terrain covered by vegetation canopy. *J Wind Eng Ind Aerodyn* 155:60-73. <https://doi.org/10.1016/j.jweia.2016.05.002>

Marciotto ER, Fisch G, Medeiros LE (2012) Characterization of surface level wind in the Centro de Lançamento de Alcântara for use in rocket structure loading and dispersion studies. *J Aerosp Technol Manag* 4(1):69-79. <https://doi.org/10.5028/jatm.2012.04014911>

Medeiros LE, Magnago RO, Fisch G, Marciotto ER (2013) Observational study of the surface layer at an ocean–land transition region. *J Aerosp Technol Manag* 5(4):449-458. <https://doi.org/10.5028/jatm.v5i4.244>

National Research Council (1998) Assessment of Exposure-Response Functions for Rocket-Emission Toxicants. Washington: National Academies Press. Appendix D, Acute toxicity of hydrogen chloride; p. 105-146. <https://doi.org/10.17226/6205>

Patankar S (1980) Numerical heat transfer and fluid flow. Boca Raton: CRC Press.

Pires LBM, Avelar AC, Fisch G, Roballo ST, Souza LF, Gielow R, Girardi RM (2009) Studies using wind tunnel to simulate the Atmospheric Boundary Layer at the Alcântara Space Center. *J Aerosp Technol Manag* 1(1):91-98. <https://doi.org/10.5028/jatm.2009.01019198>

Pires LBM, Roballo ST, Fisch G, Avelar AC, Gielow R, Girardi RM (2010) Atmospheric flow measurements using the PIV and HWA techniques. *J Aerosp Technol Manag* 2(2):127–136. <https://doi.org/10.5028/jatm.2010.02027410>

Pires LBM, Souza LF, Fisch G, Gielow R (2011) Numerical study of the atmospheric flow over a coastal cliff. *Int J Numer Methods Fluids* 67(5):599-608. <https://doi.org/10.1002/flid.2377>

Ramos DNS, Fernandez JPR, Fisch G (2018) Evolution of the Planetary Boundary Layer on the northern coast of Brazil during the CHUVA campaign. *Atmos Res* 203:298-310. <https://doi.org/10.1016/j.atmosres.2017.12.016>

Saeedi M, LePoudre PP, Wang B-C (2014) Direct numerical simulation of turbulent wake behind a surface-mounted square cylinder. *J Fluids Struct* 51:20-39. <https://doi.org/10.1016/j.jfluidstructs.2014.06.021>

Schuch D, Fisch G (2017) The use of an atmospheric model to simulate the rocket exhaust effluents transport and dispersion for the Centro de Lançamento de Alcântara. *J Aerosp Technol Manag* 9(2):137-146. <https://doi.org/10.5028/jatm.v9i2.740>

Sharma PK, Warudkar V, Ahmed S (2020) Application of a new method to develop a CFD model to analyze wind characteristics for a complex terrain. *Sustain Energy Technol Assess* 37:100580. <https://doi.org/10.1016/j.seta.2019.100580>

Shih T-H, Liou WW, Shabbir A, Yang Z, Zhu J (1995) A new $k-\epsilon$ eddy viscosity model for high Reynolds number turbulent flows. *Comput Fluids* 24(3):227-238. [https://doi.org/10.1016/0045-7930\(94\)00032-T](https://doi.org/10.1016/0045-7930(94)00032-T)

Souza BH, Fisch GF, Goulart EV (2015) Simulação do escoamento atmosférico no Centro de Lançamento de Alcântara (CLA) utilizando a técnica de CFD. Paper presented IX Workshop Brasileiro de Micrometeorologia. UFSM; Santa Maria, Brazil.

Tang X-Y, Zhao S, Fan B, Peinke J, Stoevesandt B (2019) Micro-scale wind resource assessment in complex terrain based on CFD coupled measurement from multiple masts. *Appl Energy* 238:806-815. <https://doi.org/10.1016/j.apenergy.2019.01.129>

Uchida T, Ohya Y (2003) Large-eddy simulation of turbulent airflow over complex terrain. *J Wind Eng Ind Aerodyn* 91(1-2):219-229. [https://doi.org/10.1016/S0167-6105\(02\)00347-1](https://doi.org/10.1016/S0167-6105(02)00347-1)

Wu Y, Ren H (2013) On the impacts of coarse-scale models of realistic roughness on a forward-facing step turbulent flow. *Int J Heat Fluid Flow* 40:15-31. <https://doi.org/10.1016/j.ijheatfluidflow.2013.01.015>

Yan BW, Li QS, He YC, Chan PW (2016) RANS simulation of neutral atmospheric boundary layer flows over complex terrain by proper imposition of boundary conditions and modification on the $k-\epsilon$ model. *Environ Fluid Mech* 16(1):1-23. <https://doi.org/10.1007/s10652-015-9408-1>

Yang X, Pakula M, Sotiropoulos F (2018) Large-eddy simulation of a utility-scale wind farm in complex terrain. *Appl energy* 229:767-777. <https://doi.org/10.1016/j.apenergy.2018.08.049>

Yim SHL, Fung JCH, Ng EYY (2014) An assessment indicator for air ventilation and pollutant dispersion potential in an urban canopy with complex natural terrain and significant wind variations. *Atmos Environ* 94:297-306. <https://doi.org/10.1016/j.atmosenv.2014.05.044>